Journal of Photochemistry & Photobiology A: Chemistry 400 (2020) 112666

Contents lists available at ScienceDirect

Journal of Photochemistry & Photobiology A: Chemistry

journal homepage: www.elsevier.com/locate/jphotochem

$H_2Ti_3O_7$ nanowires as a high-performance photocatalytic and surface-enhanced Raman scattering substrate

Yu-Cheng Chang[a,*], Jai-Cing Lin[a], Chia-Man Chou[b,c]

[a] Department of Materials Science and Engineering, Feng Chia University, Taichung, 40724, Taiwan
[b] Department of Surgery, Taichung Veterans General Hospital, Taichung, 40705, Taiwan
[c] College of Medicine, National Yang-Ming University, Taipei, 11221, Taiwan

ARTICLE INFO

Keywords:
$H_2Ti_3O_7$ nanowires
Hydrothermal
Ion- exchange
Photocatalytic activity
Radical-trapping
Surface-enhanced raman scattering

ABSTRACT

In the present work, we reported one kind of photocatalytic and surface-enhanced Raman scattering substrate, $H_2Ti_3O_7$ nanowires, which prepared on the Ti foil by the hydrothermal and ion-exchange methods. The morphologies, crystal structures, chemical compositions, optical properties of the as-prepared substrates investigated via the different kinds of characterization techniques. $H_2Ti_3O_7$ nanowires revealed remarkably enhanced visible-light photocatalytic activity for the degradation of rhodamine 6 G solution compared to $Na_2Ti_3O_7$ nanowires, TiO_2 nanowires, and commercial photocatalysts (TiO_2 and ZnO nanoparticles). These results attributed to the $H_2Ti_3O_7$ nanowires with a higher concentration of oxygen vacancies can enhance the visible-light absorbance, resulting in the higher photocatalytic activity under the visible-light irradiation. The radical-trapping test shows that holes and hydroxyl radicals played central roles in rhodamine 6 G photodegradation. The deposition of Ag nanoparticles on the $H_2Ti_3O_7$ nanowires can also use as a highly sensitive surface-enhanced Raman scattering substrate for detecting rhodamine 6 G solution with a concentration as low as 10^{-9} M by the ion-sputtering system.

1. Introduction

It is the first time that Fujishima and Honda employed titanium dioxide (TiO_2) for the photocatalytic decomposition of water under ultraviolet (UV) light irradiation in 1972 [1]. Since then, TiO_2 has widely used in different fields, such as photocatalytic degradation of organic pollutants, water splitting, photocatalytic reduction of carbon dioxide into fuels, dye-sensitized solar cells, supercapacitors, lithium-ion batteries, and biomedical devices [2–4]. There are three common crystal structures, such as anatase (tetragonal), rutile (tetragonal), and brookite (orthorhombic) [5]. Among them, anatase TiO_2 has extensively accepted to possess superior photocatalytic activity due to its rapid hole trapping process [6]. TiO_2 is a very important semiconductor material with a wide direct bandgap (3.2 eV for anatase, 3.0 eV for rutile, and brookite for 2.96 eV) and high light refraction coefficient (anatase n = 2.55, rutile n = 2.72, and brookite n = 2.64), resulting in its widespread of optical applications [3,7]. Also, TiO_2 is an ideal photocatalysis for practical applications on the wastewater treatments due to its strong oxidizing power, non-toxic, low-cost, and excellent chemical stability [8]. In general, a high-performance photocatalysis requires not only high surface-active sites to harvest light but also an efficient architecture prolonging photogenerated carrier lifetime to enhance their contribution in the photocatalytic process [9]. However, TiO_2 has exhibited the fast recombination ratio of photoinduced electron-hole pairs and only absorb 3–5 % of the solar spectrum, which was severe limits the photocatalytic efficiencies.

Up to now, several strategies have utilized to improve the visible-light photocatalytic performance of TiO_2. These approaches can mainly categorize into: (1). Doping metal or non-metal ions (such as C, N, and B) [10–12], (2). Deposition of noble metals [13,14], (3). Combining TiO_2 with other semiconductor materials [6,15–17], and (4) Other titanium oxide-based materials [18–21]. Among various approaches, hydrogen trititanate ($H_2Ti_3O_7$) of other titanium oxide-based materials has attracted significant interest due to their unique physical and chemical properties for applications in photocatalytic degradation of organic pollutants [22,23], water splitting [24,25], H_2 and CO_2 adsorption [26,27], dye-sensitized solar cells [28], supercapacitors [29], and Na ion batteries [30]. Also, $H_2Ti_3O_7$ is an important intermediate product of the transformation between $Na_2Ti_3O_7$ and TiO_2. The prepared powder-type of $H_2Ti_3O_7$ nanostructures with a higher surface-to-volume ratio can enhance high-performance photocatalytic activity [22,23]. However, in a practical photocatalytic process, the separation

* Corresponding author.
E-mail address: yuchchang@fcu.edu.tw (Y.-C. Chang).

https://doi.org/10.1016/j.jphotochem.2020.112666
Received 14 October 2019; Received in revised form 29 May 2020; Accepted 30 May 2020
Available online 04 June 2020

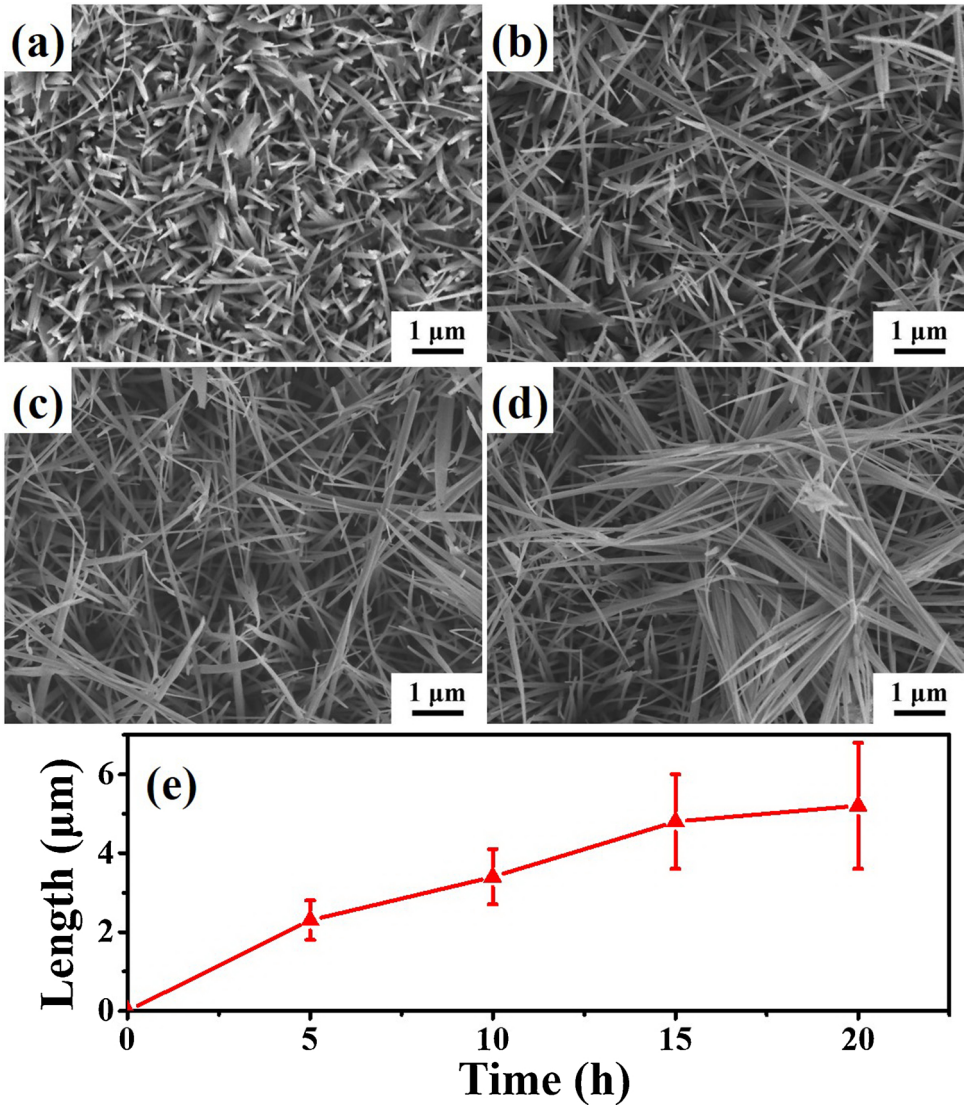

Fig. 1. (a–d) The top-view FESEM images of $Na_2Ti_3O_7$ nanowires prepared on the Ti foil at the different reaction times. The reaction times were (a) 5, (b) 10, (c) 15, and (d) 20 h, respectively. (e) The average length of $Na_2Ti_3O_7$ nanowires as a function of the reaction time.

of these powder photocatalysts from solution after reaction could be complicated, and meanwhile, the tendency to agglomerate into larger powders results in a reduction of the photocatalytic activity during the cycling use [31]. If $H_2Ti_3O_7$ nanostructures can directly grow on the solid substrates, which improve these drawbacks. However, there are fewer reports about the growth of $H_2Ti_3O_7$ nanowires on the solid substrates for the application in photocatalytic degradation of organic pollutants. To the best of our knowledge, there are no reports about the growth of $H_2Ti_3O_7$ nanowires for photocatalytic and surface-enhanced Raman scattering applications.

In this work, $H_2Ti_3O_7$ nanowires have directly synthesized on the Ti foil by simple hydrothermal and ion-exchange processes. The reaction conditions play essential roles in controlling the morphology and size of $H_2Ti_3O_7$ nanostructures. $H_2Ti_3O_7$ nanowires with more enormous amounts of surface oxygen deficiencies formation can enhance the visible-light absorbance, improving their photocatalytic activity under visible-light irradiation. Also, $H_2Ti_3O_7$ nanowires have suitable geometric structures for deposition three-dimensional Ag nanoparticles, which led to high-performance surface-enhanced Raman scattering (SERS) detection.

2. Experimental

2.1. Synthesis of $H_2Ti_3O_7$ nanowires

Titanium foil (Ti, 99.5 % pure and 0.25 mm thick, Alfa Aesar) was ultrasonically cleaned in ethanol and dilute hydrogen chloride (1 M, HCl) solution for 15 min and 1 min to remove organic contamination and oxide layer on the surface, respectively. For $Na_2Ti_3O_7$ nanowires, this substrate was placed in a separate 50 mL Teflon-lined stainless steel autoclave and filled with the different concentrations of NaOH solution (20 mL) at 220 °C for the different reaction time. For $H_2Ti_3O_7$ nanowires, this substrate with $Na_2Ti_3O_7$ nanowires washed with deionized water and ethanol in turn, then immersed in 1 M HCl solution for

30 min to replace Na^+ with H^+. Finally, this substrate was washed with deionized water and ethanol in turn, then dried under an air purge.

2.2. Characterization

The surface morphology of as-prepared photocatalysts studied with a field-emission scanning electron microscopy (FE-SEM, Hitachi S-4800) operating at 10 kV accelerating voltage. A field-emission transmission electron microscopy (FE-TEM, JEOL-2100 F) operating at 200 kV was used to examine the $H_2Ti_3O_7$ nanowire. The crystallinity of the as-prepared photocatalysts examined by using an X-ray diffractometer (XRD, Bruker D2 phaser) equipped with a Cu-Kα radiation source (λ = 0.15406 nm). Excited as-prepared photocatalysts conducted the photoluminescence (PL) spectra with a 325 nm He-Cd laser. X-ray photoelectron spectroscopy (XPS) analysis was carried out by using a ULVAC-PHI PHI 5000 Versaprobe II system equipped with an Al-Kα radiation source. The photocatalytic activities of as-prepared photocatalysts and commercial photocatalysts investigated for the degradation of rhodamine 6 G (R6G) solution (0.02 mM) without adjusting the pH value. For the photocatalytic process, UVC (Philip, 10 W, λ_{max} = 254 nm) and blue light LED (100 W, λ_{max} = 465 nm) lamps used as a source of UV and visible light, respectively. The concentration of the R6G solution was analyzed by recording variations in the characteristic absorption band (λ_{max} = 526 nm) using a UV/VIS spectroscopy (U-2900, Hitachi). The photocatalytic efficiency of as-prepared photocatalysts and commercial photocatalysts (TiO_2 nanopowder and ZnO nanopowder) under UV- or visible-light irradiation defined as C/C_0, C_0 and C were the initial and instantaneous concentrations of R6G solution, respectively. The SERS spectra analyzed by using a confocal Raman spectrometer (MRI532S, Protrustech, Taiwan) with an excitation wavelength of 532 nm and a power of 1 mW.

3. Results and discussion

3.1. Synthesis and characterization of $H_2Ti_3O_7$ nanowires

Fig. 1a–d shows the top-view FESEM micrographs of $Na_2Ti_3O_7$ nanowires were directly grown on the Ti foil by a facile hydrothermal method at 220 °C for the different reaction time. The reaction time was 5, 10, 15, and 20 h, respectively. With the increased reaction time, more and more scattered $Na_2Ti_3O_7$ nanowires formed, and some nanowires exhibited agglomeration. The average lengths of $Na_2Ti_3O_7$ nanowires were 2.3 ± 0.5, 3.4 ± 0.7, 4.8 ± 1.2, and 5.2 ± 1.6 μm, respectively, as shown in Fig. 1e. As the reaction time increased, the length deviation of $Na_2Ti_3O_7$ nanowires became more and more evident. On the other hand, appropriate reaction time cannot only be beneficial to the growth of $Na_2Ti_3O_7$ nanowires with the uniform length but also avoid forming the scattered $Na_2Ti_3O_7$ nanowires. To adequately understand the growth mechanism of $Na_2Ti_3O_7$ nanowires, the present work explored the change of the morphology under the shorter reaction time. Fig. S1 shows the 45° tilt-view FESEM micrographs of $Na_2Ti_3O_7$ nanowires were grown at a different reaction time of 1, 2, 3, 4, and 5 h, respectively. At the reaction time of 1 and 2 h, an apparent morphology of $Na_2Ti_3O_7$ nanosheets observed. When the reaction time increased, the morphology of $Na_2Ti_3O_7$ nanostructures could change from nanosheet to nanotubes. At the reaction time of 5 h, the morphology of $Na_2Ti_3O_7$ nanostructures could change from nanotubes to nanowires. Based on the SEM results, the appropriate reaction time can beneficial to grow $Na_2Ti_3O_7$ nanowires on the Ti foil.

In the previous study, the ion-exchange method can use to replace the Na^+ ions with H^+ ions on the $Na_2Ti_3O_7$ nanowires by immersed in 1 M HCl solution for 30 min [32]. Also, the $H_2Ti_3O_7$ nanowires can easily convert to TiO_2 nanowires by thermal annealing process at 500 °C for 3 h under the ambient condition [18]. Fig. 2a shows the optical photographs of $Na_2Ti_3O_7$, $H_2Ti_3O_7$, and TiO_2 nanowires grown on the Ti foils (1.5 cm × 2.5 cm) at the reaction time of 5 h. The surface color of the three kinds of crystal phase substrates cannot exhibit evidence change. Fig. 2b–d shows the 45° tilt-view FESEM micrographs of $Na_2Ti_3O_7$, $H_2Ti_3O_7$, and TiO_2 nanowires grown on the Ti foils, respectively. The average sizes of $Na_2Ti_3O_7$, $H_2Ti_3O_7$, and TiO_2 nanowires were 84.2 ± 15.6, 87.4 ± 17.1, and 86.8 ± 18.7 nm, respectively. The $H_2Ti_3O_7$ and TiO_2 nanowires cannot observe an evident change in the morphology and size of $Na_2Ti_3O_7$ nanowire after ion-exchange and thermal annealing processes. Fig. 2e shows the TEM micrograph of $H_2Ti_3O_7$ nanowires with a diameter of 76.3 nm. Fig. 2f shows the HRTEM micrograph of the $H_2Ti_3O_7$ nanowire, which a lattice spacing of 0.186 nm observed for the monoclinic $H_2Ti_3O_7$ crystal of (020) plane (JCPDS No. 41-0192).

To further determine the crystal structure and possible phase transformation during ion-exchange and thermal annealing processes, X-ray diffraction spectra of the $Na_2Ti_3O_7$, $H_2Ti_3O_7$, and TiO_2 nanowires collected in Fig. 3. Fig. 3a shows the $Na_2Ti_3O_7$ nanowires revealed two mixed diffraction peaks, containing hexagonal Ti crystal (JCPDS Card No. 44-0148) and monoclinic $Na_2Ti_3O_7$ crystal (JCPDS Card No. 44-0148), respectively. After the ion exchange process, the diffraction peaks of $Na_2Ti_3O_7$ nanowires disappeared, and three new diffraction peaks emerged at 2θ values of 24.5°, 27.1°, and 48.7° corresponding to (110), (40 − 2), and (020) crystal planes of monoclinic $H_2Ti_3O_7$ crystal (JCPDS Card No. 41-0192), as shown in Fig. 3b. This result consisted of the above HRTEM micrograph (Fig. 2f). X-ray photoelectron spectroscopy (XPS) was employed to analyze the chemical composition and bonding configuration of $H_2Ti_3O_7$ nanowires. Fig. S2 shows the XPS spectrum of $H_2Ti_3O_7$ nanowires, which mainly composed of Ti and O. The C 1s peak ascribed to the hydrocarbons from the XPS instrument itself. Also, the Na 1s peak (Fig. S2 inset) of $H_2Ti_3O_7$ nanowires disappeared after the ion exchange process. This phenomenon also indicates that $Na_2Ti_3O_7$ nanowires have successfully transformed into $H_2Ti_3O_7$ nanowires. Fig. 3c indicates that the diffraction peaks of $H_2Ti_3O_7$ nanowires, which completely converted to anatase TiO_2 crystal (JCPDS Card No. 21-1272) and rutile TiO_2 crystal (JCPDS Card No. 21-1276) by thermal annealing process at 500 °C for 6 h in ambient conditions.

To explore the energy band and electronic structures of the as-prepared photocatalysts, we investigated by the room temperature of photoluminescence (PL). Fig. 4 shows the PL spectra of $Na_2Ti_3O_7$, $H_2Ti_3O_7$, and TiO_2 nanowires grown on the Ti foil. For $Na_2Ti_3O_7$ and $H_2Ti_3O_7$ nanowires, there was exhibited a great and broad visible emission peak at 486.9 nm. The visible emission peak ascribed to the existence of surface defects or oxygen vacancies on the crystal [18,33,34]. Compared with $Na_2Ti_3O_7$ nanowires, $H_2Ti_3O_7$ nanowires could present a higher number of surface defects or oxygen vacancies to reveal the stronger visible emission.

To investigate the surface oxidation states of $Na_2Ti_3O_7$ and $H_2Ti_3O_7$ nanowires, the XPS was employed to analyze, as shown in Fig. S3. There were three peaks located at 530.4, 531.2, and 532.7 eV for the O1 s spectra, which ascribed to the lattice oxygen (O_L), oxygen vacancies or defect (O_V), and chemisorbed or dissociated oxygen (O_C) in the $Na_2Ti_3O_7$ and $H_2Ti_3O_7$ nanowires. For oxygen vacancies or defects peak at 531.2 eV, the relative intensity of $H_2Ti_3O_7$ nanowires is higher than $Na_2Ti_3O_7$ nanowires [18,35]. This result indicates that the ion-exchange process may induce the formation of oxygen vacancies or defects on the $H_2Ti_3O_7$ nanowires. For TiO_2 nanowires, there was

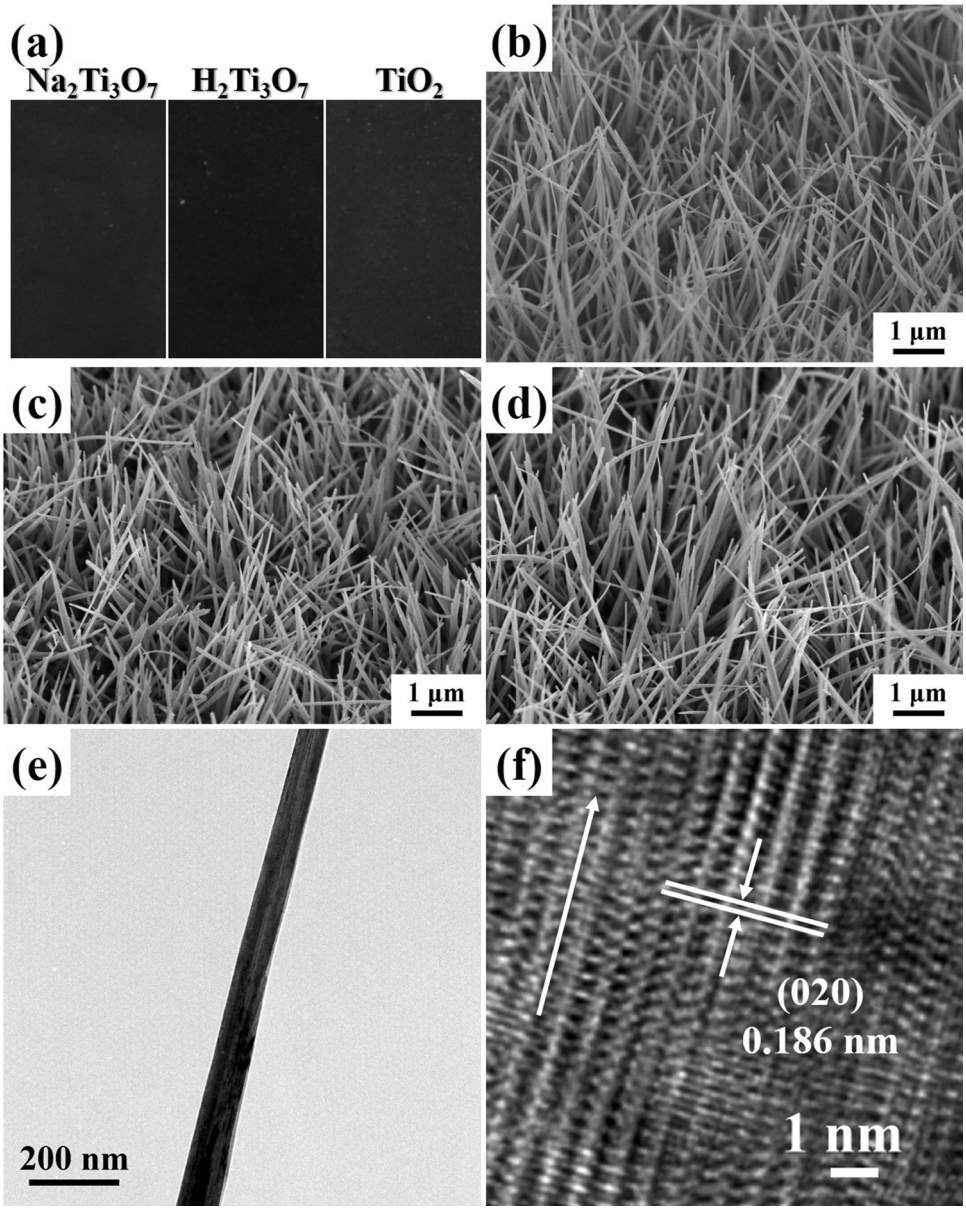

Fig. 2. (a) Optical photographs of a piece of $Na_2Ti_3O_7$, $H_2Ti_3O_7$ and, TiO_2 nanowires prepared on the Ti foil. The tilt-view FESEM images of (b) $Na_2Ti_3O_7$, (c) $H_2Ti_3O_7$, and (d) TiO_2 nanowires prepared on the Ti foil. (e) The TEM image of an $H_2Ti_3O_7$ nanowire in (c). (f) The HRTEM image of a single crystalline phase of $H_2Ti_3O_7$ nanowire in (e).

exhibited a weak and broad visible emission peak at 476.7 nm. TiO_2 nanowires exhibited a blue-shifted emission peak in comparison with $Na_2Ti_3O_7$ and $H_2Ti_3O_7$ nanowires, which shall attribute to the radiative recombination of the photogenerated holes with the electrons occupying the oxygen vacancies to form singly ionized oxygen vacancies [36]. $H_2Ti_3O_7$ nanowires with a high concentration of oxygen vacancies can not only act the positive charge centers to trap electrons but also create an impurity level near the valence band to induce the bandgap narrowing [37]. These results shall be beneficial to enhance the visible-light photocatalytic activity.

3.2. Photocatalytic activity of $H_2Ti_3O_7$ nanowires

The photocatalytic performance of $Na_2Ti_3O_7$ nanowires grown with the different reaction times in the same area (1.5 cm × 2.5 cm) evaluated by the degradation of R6G solution under low-powered UVC lamp (10 W). Fig. 5a shows the ratio (C/C_0) of the concentration of R6G solution (C) and initial R6G solution (C_0) versus the irritation time [38]. The photocatalytic efficiency of blank (without photocatalysts) and $Na_2Ti_3O_7$ nanowires grown with the different reaction times were 13.5, 81.9 (5 h), 79.7 (10 h), 79.1 (15 h), and 80.3 % (20 h), respectively. When the reaction time exceeded 5 h, the photocatalytic efficiency of $Na_2Ti_3O_7$ nanowires tended to decrease. This phenomenon attributed the surface of $Na_2Ti_3O_7$ nanowires with scattered $Na_2Ti_3O_7$ nanowires, which could decrease the surface active sites of photocatalysts. Fig. 5b depicts that the photocatalytic efficiency of $Na_2Ti_3O_7$, $H_2Ti_3O_7$, and TiO_2 nanowires grown at the reaction time of 5 h were 81.9, 82.8, and 75 %, respectively. Compared with TiO_2 nanowires, the $Na_2Ti_3O_7$ and $H_2Ti_3O_7$ nanowires revealed to enhance photocatalytic efficiency under a low-powered UVC lamp. These results ascribe to $Na_2Ti_3O_7$ and $H_2Ti_3O_7$ nanowires with a high concentration of oxygen vacancies, which can reduce the recombination rate of electron-hole pairs to increase the photocatalytic efficiency under the UVC irradiation.

Fig. 5c shows the photocatalytic efficiency of as-prepared and commercial photocatalysts under the visible-light irradiation. The blank experiment indicates that the photodegradation of R6G was negligible

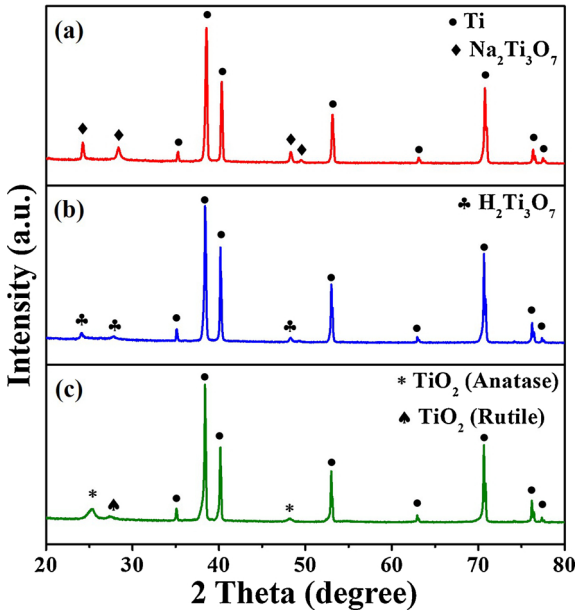

Fig. 3. XRD spectra of (a) $Na_2Ti_3O_7$, (b) $H_2Ti_3O_7$, and (c) TiO_2 nanowires prepared on the Ti foil.

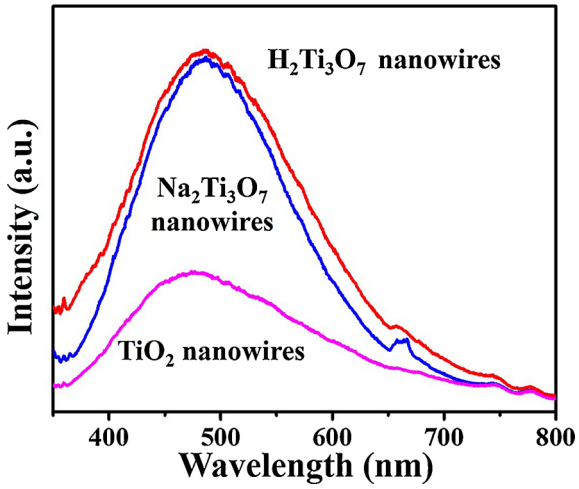

Fig. 4. PL spectra of $Na_2Ti_3O_7$, $H_2Ti_3O_7$, and TiO_2 nanowires fabricated on the Ti foil.

in the absence of photocatalysts under the visible-light irradiation. The photocatalytic efficiency of blank (without photocatalysts), as-prepared photocatalysts ($Na_2Ti_3O_7$, $H_2Ti_3O_7$, TiO_2 nanowires grown on the Ti foil), commercial photocatalysts (TiO_2 and ZnO nanoparticles) were 2.4 (blank), 79.5 ($Na_2Ti_3O_7$ nanowires), 94 ($H_2Ti_3O_7$ nanowires), 3.9 (TiO_2 nanowires), 29.3 (TiO_2 nanoparticles), and 52.2 % (ZnO nanoparticles), respectively. The photocatalytic efficiency of $H_2Ti_3O_7$ nanowires exhibited superior compared with other as-prepared and commercial photocatalysts. The photocatalytic degradation kinetics of R6G solution followed a pseudo-first-order reaction, and the reaction constants were calculated to be 0.0001 (blank), 0.0086 ($Na_2Ti_3O_7$ nanowires), 0.0160 ($H_2Ti_3O_7$ nanowires), 0.0002 (TiO_2 nanowires), 0.0017 (TiO_2 nanoparticles), and 0.0037 min^{-1} (ZnO nanoparticles), respectively, as shown Fig. 5d. For as-prepared photocatalysts, $H_2Ti_3O_7$ nanowires revealed almost 1.8 and 80 times higher than that of $Na_2Ti_3O_7$ nanowires and TiO_2 nanowires, respectively. For commercial photocatalysts, $H_2Ti_3O_7$ nanowires exhibited almost 9.4 and 4.3 times higher than that of TiO_2 nanoparticles and ZnO nanoparticles, respectively. This phenomenon may attribute to $H_2Ti_3O_7$ nanowires with a high concentration of oxygen vacancies, which can induce bandgap narrowing for improving visible-light photocatalytic degradation.

To investigate the photocatalytic mechanism in the R6G photodegradation process, four kinds of radical scavengers added into photocatalytic reaction. In the present work, benzoquinone (BQ), silver nitrate ($AgNO_3$), isopropyl alcohol (IPA), and triethanolamine (TEOA) were used as radical scavengers to quench superoxide radical anions ($^{\cdot}O_2$–), electrons (e–), hydroxyl radicals (·OH), and holes (h^+), respectively. The decrease in the photocatalytic efficiency of $H_2Ti_3O_7$ nanowires can use to evaluate the importance of radical scavengers. Fig. 6a shows the variation of photocatalytic efficiency of $H_2Ti_3O_7$ nanowires was accompany by the addition of different kinds of radical scavengers. It is evident that with no radical scavengers, the photocatalytic efficiency of $H_2Ti_3O_7$ nanowires was 93.2 %. When the reaction solution added radical scavengers of BQ, $AgNO_3$, IPA, and TEOA, the photocatalytic efficiency of $H_2Ti_3O_7$ nanowires decreased to 39.4, 38.7, 26.3, and 21.9, respectively. This result indicates that h^+ and ·OH played the mainly important radicals for the photodegradation of R6G.

Based on the above results, the possible photocatalytic mechanism of $H_2Ti_3O_7$ nanowires under the visible-light irradiation can illustrate in Fig. 6b. The conduction band (CB) and valance band (VB) of $H_2Ti_3O_7$ are positioned at −0.084 and 3.216 V, respectively [21,39]. The oxygen vacancy can create a new electric state band at the bottom of the CB of $H_2Ti_3O_7$ nanowires, which couples with narrowing the bandgap to improve the visible-light absorption. The oxygen vacancy induced visible-light absorption and enhanced photocatalytic performances have been reported in the different kinds of metal oxide materials [33,37,40–43]. In this study, the photogenerated electrons of $H_2Ti_3O_7$ nanowires shall be excited into their CB under the visible-light irradiation. The photogenerated electrons (e–) can reduce O_2 molecules to H_2O_2 and finally into hydroxyl radicals (HO·) for the degradation of R6G solution. The photogenerated holes (h^+) in the VB of $H_2Ti_3O_7$ nanowires can directly react with R6G solution or indirectly react with H_2O molecules to form hydroxyl radicals (HO·) for the degradation of R6G solution. The photocatalytic degradation process can be described as follows [44–47]

$$H_2Ti_3O_7 + h\nu \rightarrow e^- (H_2Ti_3O_7, CB) + h^+ (H_2Ti_3O_7, VB)$$

$$h^+ + H_2O \rightarrow HO^{\cdot} + H^+$$

$$O_2 + 2H^+ + 2e^- \rightarrow H_2O_2$$

$$H_2O_2 + h^+ \rightarrow HO_2^{\cdot} + H^+$$

$$HO_2^{\cdot} + OH^- \rightarrow O_2^{\cdot -} + H_2O$$

$$O_2^{\cdot -} + 2H^+ + e^- \rightarrow H_2O_2$$

$$H_2O_2 + h\nu \rightarrow 2HO^{\cdot}$$

$$h^+ \text{ or } HO^{\cdot} + R6G \rightarrow \text{Photodegradation products}$$

The recyclability and stability of the photocatalyst was a critical factor for its practical application. Fig. 7 shows the recycling photodegradation of the R6G solution to test the stability of $H_2Ti_3O_7$ nanowires under the visible-light irradiation. The photocatalytic efficiency of $H_2Ti_3O_7$ nanowires was respectively 94.0, 92.3, 92.0, 89.9, and 91.8 % for the five cycles. After the recyclability tests, the photocatalytic efficiency of $H_2Ti_3O_7$ nanowires revealed an insignificant decrease (~2.3 %), which could ascribe to them directly grown on the Ti foil with unavoidable loss in the photodegrading process. Also, the XRD spectrum (Fig. S4) of the recycled $H_2Ti_3O_7$ nanowires were almost similar to the fresh photocatalysts (Fig. 3b). $H_2Ti_3O_7$ nanowires exhibited excellent stability in the photodegrading process under the visible-light irradiation, which shall be a promising role in the wastewater treatment.

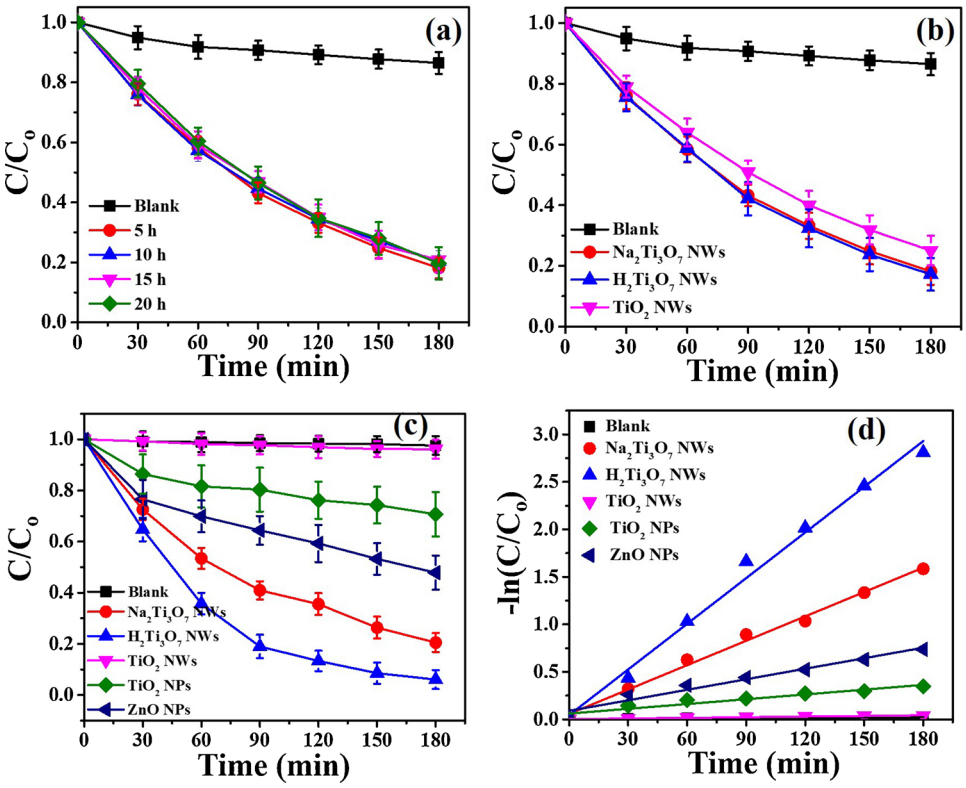

Fig. 5. (a) Photocatalytic properties of $Na_2Ti_3O_7$ nanowires prepared on the Ti foil at the different reaction times under the UVC lamp. (b) Photocatalytic properties of $Na_2Ti_3O_7$, $H_2Ti_3O_7$, and TiO_2 nanowires prepared on the Ti foil under the UVC lamp. (c) Photocatalytic properties of different photocatalysts under the blue-light LED lamp. (d) Kinetic simulation curves of R6 G degradation over (c).

3.3. Surface-enhanced Raman scattering of $H_2Ti_3O_7$ nanowires

Due to $H_2Ti_3O_7$ nanowires directly aligned on the Ti foil, which could be beneficial to decorate Ag nanoparticles form three-dimensional $H_2Ti_3O_7$@Ag heterostructures for the application of surface-enhanced Raman scattering. Fig. 8a shows the 45° tilt-view FESEM image of $H_2Ti_3O_7$ nanowires have been wholly decorated Ag nanoparticles by the ion-beam sputtering system at the sputtering duration of 60 s. The TEM image (Fig. 8b) of an individual $H_2Ti_3O_7$@Ag heterostructure further confirms that Ag nanoparticles have covered on the $H_2Ti_3O_7$ nanowires to make the surface rougher. Fig. 8c shows the HRTEM image of an Ag nanoparticle on the surface of $H_2Ti_3O_7$ nanowire, which two distinct regions of lattice fringes observed. One was a lattice spacing of 0.186 nm observed for the monoclinic $H_2Ti_3O_7$ crystal of (020) plane (JCPDS No. 41-0192). The other was a lattice spacing of 0.235 nm observed for the cubic Ag crystal of (111) plane (JCPDS No. 04-0783). Fig. 8 d–f shows the EDS mapping images of an $H_2Ti_3O_7$@Ag heterostructure were Ti, O, and Ag, respectively. It can observe that Ti, O, and Ag dominated the composition of $H_2Ti_3O_7$@Ag heterostructure.

To estimate the SERS activity of $H_2Ti_3O_7$@Ag heterostructures through detecting the Raman vibrational signals of R6G molecules, we compared the behaviors of Ag nanoparticle decorated on the $H_2Ti_3O_7$ nanowires with a different sputtering time of 15, 30, 60, and 90 s, respectively. $H_2Ti_3O_7$@Ag heterostructures immersed into the R6G solution (10^{-6} M) at room temperature for 1 h in the dark and dried with N_2 purge. Fig. 9a presents the SERS spectra of R6G molecules adsorbed

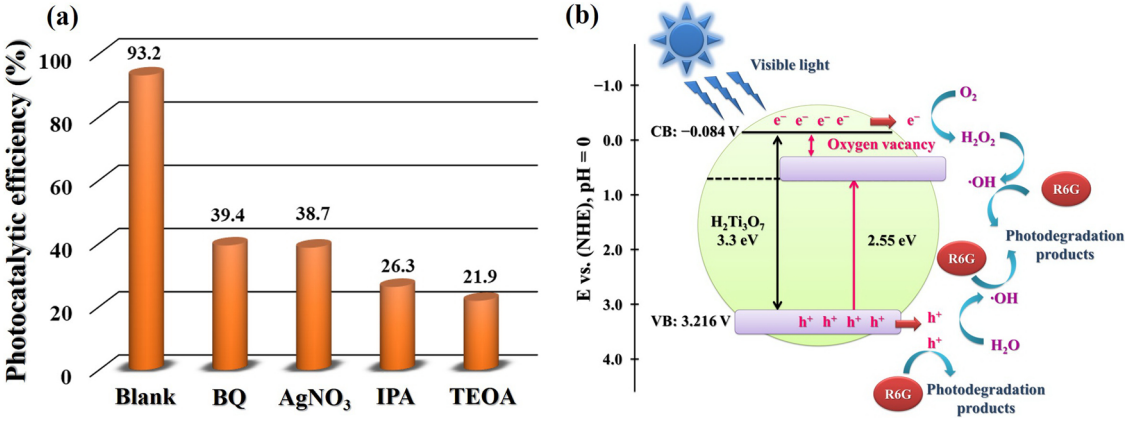

Fig. 6. (a) The photodegradation of R6 G solution on the Ti foil with $H_2Ti_3O_7$ nanowires in the presence of various scavengers. (b) The schematic diagram for photocatalytic degradation of R6 G solution by $H_2Ti_3O_7$ nanowires.

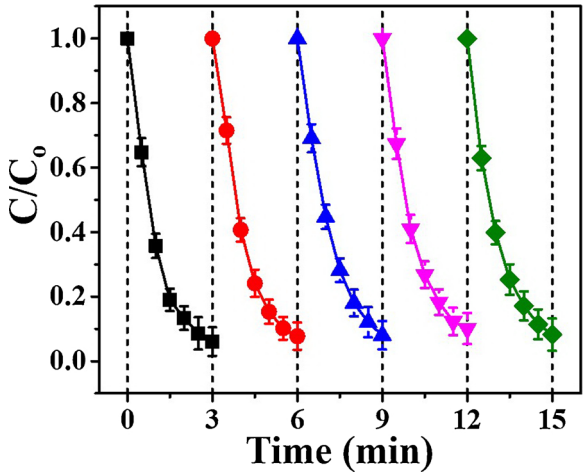

Fig. 7. The reusability test of the $H_2Ti_3O_7$ nanowires prepared on the Ti foil for the photodegradation of R6 G solution under blue-light LED lamp.

on the $H_2Ti_3O_7$@Ag heterostructures fabricated using a different sputtering time. The main Raman peaks assigned to the R6G molecules, such as 1127, 1183, 1310, 1363, 1509, 1575, and 1645 cm^{-1} [48,49]. The SERS intensity of the $H_2Ti_3O_7$@Ag heterostructures increased significantly with an increase in the sputtering time, wherein the highest SERS intensity achieved at the sputtering time of 60 s. The SERS intensity of the $H_2Ti_3O_7$@Ag heterostructures decreased at the sputtering time of 90 s, which was ascribed to the aggregation of Ag nanoparticles during the long sputtering time to reduce the number of hot spots in the three-dimensional structures. Fig. 9b presents the SERS spectra of R6G solution adsorbed on the $H_2Ti_3O_7$@Ag heterostructures with the sputtering time of the 60 s at the different concentrations (10^{-6} to 10^{-9} M). The intensity of all of the Raman peaks decreased sharply with the decrease in the concentration of R6 G solution. The lowest detected concentration of R6G solution was 10^{-9} M. This result demonstrates that the $H_2Ti_3O_7$@Ag heterostructures can use in the highly sensitive SERS-base sensing. In our previous work, semiconductor nanostructures with Ag nanoparticles could use to improve photocatalytic efficiency, which attributed to the rapid photoinduced charge separation, more photo-absorption in the visible region, and surface active sites [50]. $H_2Ti_3O_7$@Ag heterostructures with a different sputtering time also used to photodegrade the R6G solution under the visible-light irradiation, as shown in Fig. S5. Accompany with the increase in the sputtering time of Ag nanoparticles, the photocatalytic efficiency of $H_2Ti_3O_7$@Ag heterostructures gradually decreased. This phenomenon should reasonably attribute to the fact that the high-density Ag nanoparticles may reduce light penetration into $H_2Ti_3O_7$ nanowires and inhibit their photocatalytic activity.

4. Conclusions

In summary, $H_2Ti_3O_7$ nanowires have successfully prepared on the Ti foil via the combination of hydrothermal and ion-exchange processes. $H_2Ti_3O_7$ nanowires exhibited very prominent blue emission from surface oxygen vacancies in the PL spectrum. $H_2Ti_3O_7$ nanowires can beneficial to enhance photocatalytic decomposition of R6G solution under visible-light irradiation. Compare with $Na_2Ti_3O_7$ nanowires and TiO_2 nanowires, $H_2Ti_3O_7$ nanowires with large amounts of oxygen vacancies or surface defects can improve the light-harvesting ability to enhance their photocatalytic activity under visible-light irradiation. The holes and hydroxyl radicals were two main active species during the photocatalytic processes. The decorated Ag nanoparticles on the $H_2Ti_3O_7$ nanowires can also provide an excellent SERS-active substrate in the detection of the R6G solution with a concentration as low as 10^{-9} M.

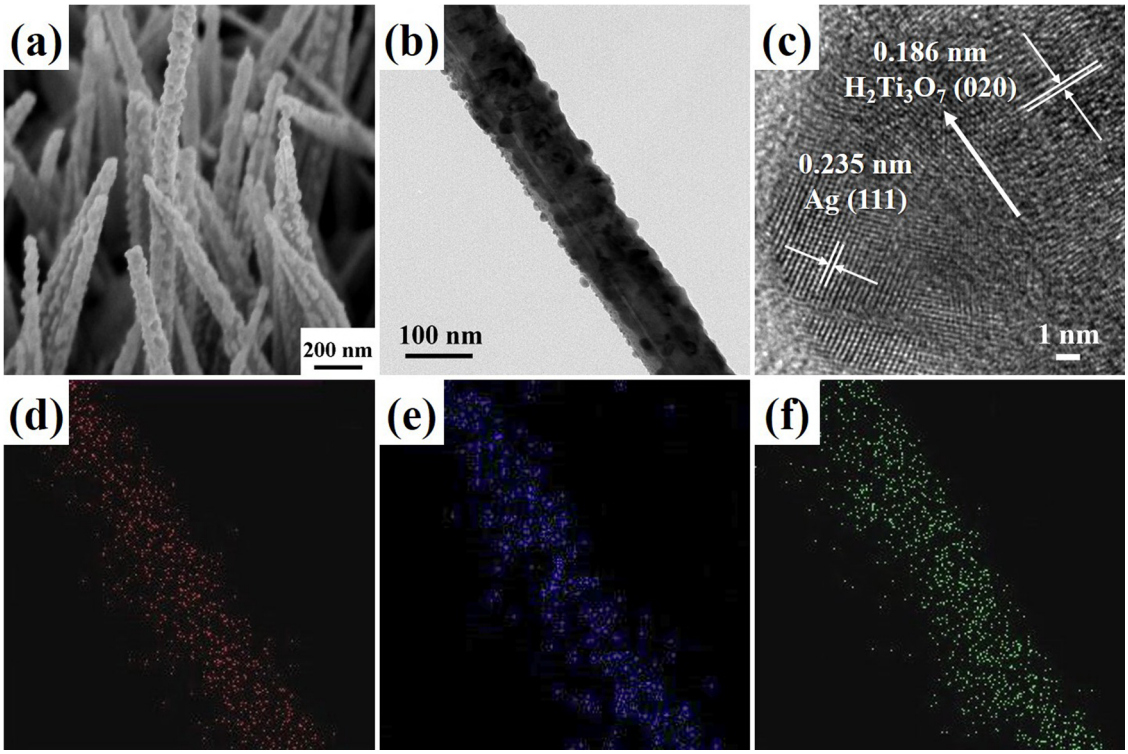

Fig. 8. (a) The tilt-view FESEM images of $H_2Ti_3O_7$ nanowires with 60 s Ag-sputtering duration prepared on the Ti foil. (b) TEM, (c) HRTEM, and (d-f) EDS mapping images of an $H_2Ti_3O_7$ nanowire. The EDS mapping images were (d) Ti, (e) O, and (f) Ag, respectively.

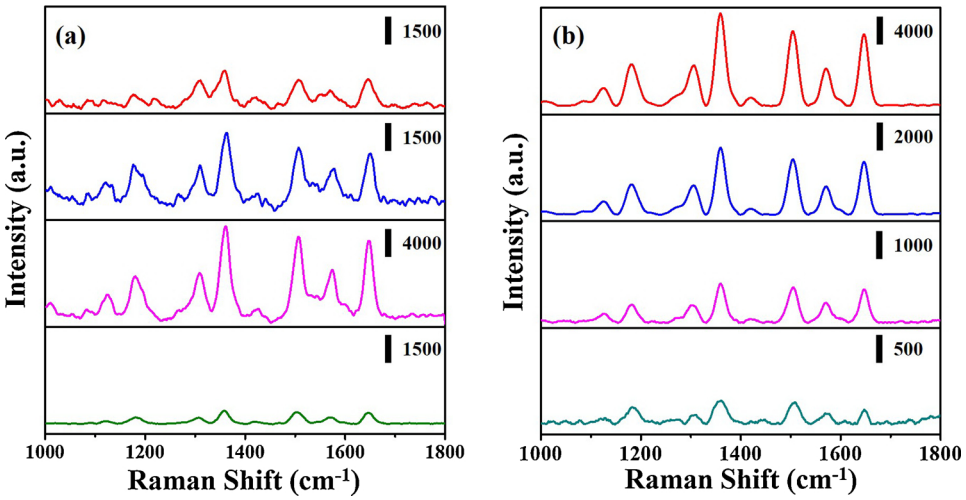

Fig. 9. (a) SERS spectra of R6 G solution (1×10^{-6} M) collected on the $H_2Ti_3O_7$ nanowires with different Ag-sputtering durations. The Ag-sputtering durations were 15, 30, 60, and 90 s, respectively. (b) SERS spectra of different concentrations of R6 G solution collected on the $H_2Ti_3O_7$ nanowires. The concentrations of R6 G solution were 10^{-6}, 10^{-7}, 10^{-8}, and 10^{-9} M, respectively.

CRediT authorship contribution statement

Yu-Cheng Chang: Conceptualization, Methodology, Software, Resources, Writing - original draft, Writing - review & editing, Visualization, Supervision, Project administration, Funding acquisition. **Jai-Cing Lin:** Validation, Formal analysis, Investigation, Data curation. **Chia-Man Chou:** Funding acquisition.

Declaration of Competing Interest

We declare that we have no financial and personal relationships with other people or organizations that can inappropriately influence our work, there is no professional or other personal interest of any nature or kind in any product, service and/or company that could be construed as influencing the position presented in, or the review of, the manuscript entitled, "$H_2Ti_3O_7$ nanowires as a high-performance photocatalytic and surface-enhanced Raman scattering substrate".

Acknowledgments

The authors gratefully acknowledge the financial support provided by the Ministry of Science and Technology, Taiwan (Grant No. MOST 106-2221-E-035-032-MY3 and MOST 108-2218-E-035-005-) and Taichung Veterans General Hospital (TCVGH-1085401C and TCVGH-FCU1088203). The authors appreciate the Precision Instrument Support Center of Feng Chia University in providing the fabrication and measurement facilities.

Appendix A. Supplementary data

Supplementary material related to this article can be found, in the online version, at doi:https://doi.org/10.1016/j.jphotochem.2020.112666.

References

[1] Y. Zhang, Z. Jiang, J. Huang, L.Y. Lim, W. Li, J. Deng, D. Gong, Y. Tang, Y. Lai, Z. Chen, Titanate and titania nanostructured materials for environmental and energy applications: a review, RSC Adv. 5 (2015) 79479–79510.
[2] P. Roy, D. Kim, K. Lee, E. Spiecker, P. Schmuki, TiO2 nanotubes and their application in dye-sensitized solar cells, Nanoscale 2 (2010) 45–59.
[3] M. Ge, C. Cao, J. Huang, S. Li, Z. Chen, K.-Q. Zhang, S.S. Al-Deyab, Y. Lai, A review of one-dimensional TiO2 nanostructured materials for environmental and energy applications, J. Mater. Chem. A 4 (2016) 6772–6801.
[4] Y. Tang, Y. Lai, D. Gong, K.H. Goh, T.T. Lim, Z. Dong, Z. Chen, Ultrafast synthesis of layered titanate microspherulite particles by electrochemical spark discharge spallation, Chem. Eur. J. 16 (2010) 7704–7708.
[5] K. Nakata, A. Fujishima, TiO2 photocatalysis: design and applications, J. Photochem. Photobiol. C 13 (2012) 169–189.
[6] B. Chen, Y. Meng, J. Sha, C. Zhong, W. Hu, N. Zhao, Preparation of MoS2/TiO2 based nanocomposites for photocatalysis and rechargeable batteries: progress, challenges, and perspective, Nanoscale 10 (2018) 34–68.
[7] J.E.S. Haggerty, L.T. Schelhas, D.A. Kitchaev, J.S. Mangum, L.M. Garten, W. Sun, K.H. Stone, J.D. Perkins, M.F. Toney, G. Ceder, D.S. Ginley, B.P. Gorman, J. Tate, High-fraction brookite films from amorphous precursors, Sci. Rep. 7 (2017) 15232.
[8] M.E. Borges, M. Sierra, J. Méndez-Ramos, P. Acosta-Mora, J.C. Ruiz-Morales, P. Esparza, Solar degradation of contaminants in water: TiO2 solar photocatalysis assisted by up-conversion luminescent materials, Sol. Energy Mater. Sol. Cells 155 (2016) 194–201.
[9] A. Ghobadi, T.G. Ulusoy, R. Garifullin, M.O. Guler, A.K. Okyay, A heterojunction design of single layer hole tunneling ZnO passivation wrapping around TiO2Nanowires for superior photocatalytic performance, Sci. Rep. 6 (2016) 30587.
[10] S. Yadav, G. Jaiswar, Review on undoped/doped TiO2 nanomaterial; synthesis and photocatalytic and antimicrobial activity, J. Chin. Chem. Soc. 64 (2017) 103–116.
[11] L. Li, Y. Yang, X. Liu, R. Fan, Y. Shi, S. Li, L. Zhang, X. Fan, P. Tang, R. Xu, W. Zhang, Y. Wang, L. Ma, A direct synthesis of B-doped TiO2 and its photocatalytic performance on degradation of RhB, Appl. Surf. Sci. 265 (2013) 36–40.
[12] X. Wu, S. Yin, Q. Dong, C. Guo, H. Li, T. Kimura, T. Sato, Synthesis of high visible light active carbon doped TiO2 photocatalyst by a facile calcination assisted solvothermal method, Appl. Catal. B 142-143 (2013) 450–457.
[13] V. Vaiano, G. Iervolino, D. Sannino, J.J. Murcia, M.C. Hidalgo, P. Ciambelli, J.A. Navío, Photocatalytic removal of patent blue V dye on Au-TiO2 and Pt-TiO2 catalysts, Appl. Catal. B 188 (2016) 134–146.
[14] M.G. Méndez-Medrano, E. Kowalska, A. Lehoux, A. Herissan, B. Ohtani, D. Bahena, V. Briois, C. Colbeau-Justin, J.L. Rodríguez-López, H. Remita, Surface modification of TiO2 with Ag nanoparticles and CuO nanoclusters for application in photocatalysis, J. Phys. Chem. C 120 (2016) 5143–5154.
[15] L. Zhan, J. He, W. Wang, X. Zheng, Y. Cao, J. Yin, L. Kong, Q. Zou, W.A. Bhutto, X. Chen, S. Li, Z. Wu, J. Kang, Optimized design of multi-shell ZnO/TiO2/ZnSe nanowires decorated with Ag nanoparticles for photocatalytic applications, RSC Adv. 6 (2016) 71800–71806.
[16] H. Yang, J. Tian, Y. Bo, Y. Zhou, X. Wang, H. Cui, Visible photocatalytic and photoelectrochemical activities of TiO2 nanobelts modified by In2O3 nanoparticles, J. Colloid Interface Sci. 487 (2017) 258–265.
[17] H. Zhao, M. Wu, J. Liu, Z. Deng, Y. Li, B.-L. Su, Synergistic promotion of solar-driven H2 generation by three-dimensionally ordered macroporous structured TiO2-Au-CdS ternary photocatalyst, Appl. Catal. B 184 (2016) 182–190.
[18] Y.-C. Chang, J.-C. Lin, S.-H. Wu, One-step growth of Na2Ti3O7 nanorods for enhanced photocatalytic activities and recyclability, J. Alloys. Compd. 749 (2018) 955–960.
[19] V. Štengl, S. Bakardjieva, J. Šubrt, E. Večerníková, L. Szatmary, M. Klementová, V. Balek, Sodium titanate nanorods: preparation, microstructure characterization and photocatalytic activity, Appl. Catal. B 63 (2006) 20–30.
[20] C.-Y. Xu, J. Wu, P. Zhang, S.-P. Hu, J.-X. Cui, Z.-Q. Wang, Y.-D. Huang, L. Zhen, Molten salt synthesis of Na2Ti3O7 and Na2Ti6O13 one-dimensional nanostructures and their photocatalytic and humidity sensing properties, CrystEngComm 15 (2013) 3448–3454.
[21] M. Du, G. Zeng, J. Huang, D. Sun, Q. Li, G. Wang, X. Li, Green photocatalytic oxidation of benzyl alcohol over noble-metal-modified H2Ti3O7 nanowires, ACS Sustain. Chem. Eng. 7 (2019) 9717–9726.
[22] P. Dong, Y. Wang, B. Liu, L. Guo, Y. Huang, S. Yin, Effect of hydrothermal reaction time on morphology and photocatalytic activity of H2Ti3O7 nanotubes obtained via a rapid synthesis route, Appl. Surf. Sci. 258 (2012) 7052–7058.
[23] Y.-C. Pu, Y.-C. Chen, Y.-J. Hsu, Au-decorated NaxH2 − xTi3O7 nanobelts exhibiting remarkable photocatalytic properties under visible-light illumination, Appl. Catal. B 97 (2010) 389–397.
[24] S.-W. Lai, J.-W. Park, S.-H. Yoo, J.-M. Ha, E.-H. Song, S.-O. Cho, Surface synergism of Pd/H2Ti3O7 composite nanowires for catalytic and photocatalytic hydrogen production from ammonia borane, Int. J. Hydrogen Energy 41 (2016) 3428–3435.

[25] K. Kiatkittipong, A. Iwase, J. Scott, R. Amal, Photocatalysis of heat treated sodium- and hydrogen-titanate nanoribbons for water splitting, H2/O2 generation and oxalic acid oxidation, Chem. Eng. Sci. 93 (2013) 341–349.
[26] S. Sim, E.-B. Cho, S. Chatterjee, H2 and CO2 uptake for hydrogen titanate (H2Ti3O7) nanotubes and nanorods at ambient temperature and pressure, Chem. Eng. J. 303 (2016) 64–72.
[27] M. Ota, Y. Hirota, Y. Uchida, Y. Sakamoto, N. Nishiyama, Low temperature synthesized H2Ti3O7 nanotubes with a high CO2 adsorption property by amine modification, Langmuir 34 (2018) 6814–6819.
[28] E. German, R. Faccio, Á.W. Mombrú, Theoretical study of new potential semiconductor surfaces performance for dye sensitized solar cell usage: TiO2-B (001), (100) and H2Ti3O7 (100), Appl. Surf. Sci. 426 (2017) 1182–1189.
[29] J. Yang, L. Lian, P. Xiong, M. Wei, Pseudo-capacitive performance of titanate nanotubes as a supercapacitor electrode, Chem. Commun. 50 (2014) 5973–5975.
[30] A. Eguía-Barrio, E. Castillo-Martínez, M. Zarrabeitia, M.A. Muñoz-Márquez, M. Casas-Cabanas, T. Rojo, Structure of H2Ti3O7 and its evolution during sodium insertion as anode for Na ion batteries, Phys. Chem. Chem. Phys. 17 (2015) 6988–6994.
[31] D. Lin, H. Wu, R. Zhang, W. Pan, Enhanced photocatalysis of electrospun Ag−ZnO heterostructured nanofibers, Chem. Mater. 21 (2009) 3479–3484.
[32] X. Peng, A. Chen, Large-scale synthesis and characterization of TiO2-based nanostructures on Ti substrates, Adv. Funct. Mater. 16 (2006) 1355–1362.
[33] X. Pan, M.-Q. Yang, X. Fu, N. Zhang, Y.-J. Xu, Defective TiO2 with oxygen vacancies: synthesis, properties and photocatalytic applications, Nanoscale 5 (2013) 3601–3614.
[34] M.-P. Lu, C.-W. Chen, M.-Y. Lu, Charge-separation kinetics of photoexcited oxygen vacancies in ZnO nanowire field-effect transistors, Phys. Rev. Appl. 6 (2016) 054018.
[35] Y.-C. Chang, C.-C. Hsu, S.-H. Wu, K.-W. Chuang, Y.-F. Chen, Fabrication of Cu-doped ZnO nanoneedles on different substrate via wet chemical approach: Structural characterization and photocatalytic performance, Appl. Surf. Sci. 447 (2018) 213–221.
[36] J. Gan, X. Lu, J. Wu, S. Xie, T. Zhai, M. Yu, Z. Zhang, Y. Mao, S.C.I. Wang, Y. Shen, Y. Tong, Oxygen vacancies promoting photoelectrochemical performance of In2O3 nanocubes, Sci. Rep. 3 (2013) 1021.
[37] J. Wang, Z. Wang, B. Huang, Y. Ma, Y. Liu, X. Qin, X. Zhang, Y. Dai, Oxygen vacancy induced band-gap narrowing and enhanced visible light photocatalytic activity of ZnO, ACS Appl. Mater. Interfaces 4 (2012) 4024–4030.
[38] Y.-C. Chang, P.-S. Lin, F.-K. Liu, J.-Y. Guo, C.-M. Chen, One-step and single source synthesis of Cu-doped ZnO nanowires on flexible brass foil for highly efficient field emission and photocatalytic applications, J. Alloys. Compd. 688 (Part B) (2016) 242–251.
[39] B. Lin, Y. Zhou, L. He, W. Yang, Y. Chen, B. Gao, Mesoporous CdS-pillared H2Ti3O7 nanohybrids with efficient photocatalytic activity, J. Phys. Chem. Solids 79 (2015) 66–71.
[40] M.J. Islam, D.A. Reddy, J. Choi, T.K. Kim, Surface oxygen vacancy assisted electron transfer and shuttling for enhanced photocatalytic activity of a Z-scheme CeO2–AgI nanocomposite, RSC Adv. 6 (2016) 19341–19350.
[41] H. Li, J. Li, Z. Ai, F. Jia, L. Zhang, Oxygen vacancy-mediated photocatalysis of BiOCl: reactivity, selectivity, and perspectives, Angew. Chem. Int. Ed. 57 (2018) 122–138.
[42] S. Kumar, A.K. Ojha, Oxygen vacancy induced photoluminescence properties and enhanced photocatalytic activity of ferromagnetic ZrO2 nanostructures on methylene blue dye under ultra-violet radiation, J. Alloys. Compd. 644 (2015) 654–662.
[43] F. Dong, X. Xiao, G. Jiang, Y. Zhang, W. Cui, J. Ma, Surface oxygen-vacancy induced photocatalytic activity of La(OH)3 nanorods prepared by a fast and scalable method, Phys. Chem. Chem. Phys. 17 (2015) 16058–16066.
[44] L.C. Sim, K.S. Koh, K.H. Leong, Y.H. Chin, A.A. Aziz, P. Saravanan, In situ growth of g-C3N4 on TiO2 nanotube arrays: construction of heterostructures for improved photocatalysis properties, J. Environ. Chem. Eng. 8 (2020) 103611.
[45] F. Dong, Q. Li, Y. Sun, W.-K. Ho, Noble metal-like behavior of plasmonic Bi particles as a cocatalyst deposited on (BiO)2CO3 microspheres for efficient visible light photocatalysis, ACS Catal. 4 (2014) 4341–4350.
[46] Y.-C. Chang, S.-H. Wu, Bi-functional Al-doped ZnO@SnO2 heteronanowires as efficient substrates for improving photocatalytic and SERS performance, J. Indust. Eng. Chem. 76 (2019) 333–343.
[47] B.R. Cruz-Ortiz, J.W.J. Hamilton, C. Pablos, L. Díaz-Jiménez, D.A. Cortés-Hernández, P.K. Sharma, M. Castro-Alférez, P. Fernández-Ibañez, P.S.M. Dunlop, J.A. Byrne, Mechanism of photocatalytic disinfection using titania-graphene composites under UV and visible irradiation, Chem. Eng. J. 316 (2017) 179–186.
[48] Y. Zhang, S. Sun, X. Zhang, L. Tang, X. Song, Z. Yang, Sulfate-ion-assisted galvanic replacement tuning of silver dendrites to highly branched chains for effective SERS, Phys. Chem. Chem. Phys. 16 (2014) 18918–18925.
[49] C. Zhu, G. Meng, Q. Huang, Z. Huang, Vertically aligned Ag nanoplate-assembled film as a sensitive and reproducible SERS substrate for the detection of PCB-77, J. Hazard. Mater. 211-212 (2012) 389–395.
[50] Y.-C. Chang, J.-Y. Guo, Double-sided plasmonic silver nanoparticles decorated copper oxide/zinc oxide heterostructured nanomaces with improving photocatalytic performance, J. Photochem. Photobiol. A: Chem. 378 (2019) 184–191.